Journal of Geophysical Research: Solid Earth

RESEARCH ARTICLE
10.1029/2018JB015909

Special Section:
Magnetism in the Geosciences - Advances and Perspectives

The Vortex State in Geologic Materials: A Micromagnetic Perspective

Ioan Lascu[1,2], **Joshua F. Einsle**[2,3], **Matthew R. Ball**[2], **and Richard J. Harrison**[2]

[1]Department of Mineral Sciences, National Museum of Natural History, Smithsonian Institution, Washington, DC, USA, [2]Department of Earth Sciences, University of Cambridge, Cambridge, UK, [3]Department of Materials Sciences and Metallurgy, University of Cambridge, Cambridge, UK

Abstract A wide variety of Earth and planetary materials are very good recorders of paleomagnetic information. However, most magnetic grains in these materials are not in the stable single domain grain size range but are larger and in nonuniform vortex magnetization states. We provide a detailed account of vortex phenomena in geologic materials by simulating first-order reversal curves (FORCs) via finite-element micromagnetic modeling of magnetite nanoparticles with realistic morphologies. The particles have been reconstructed from focused ion beam nanotomography of magnetite-bearing obsidian and accommodate single and multiple vortex structures. Single vortex (SV) grains have fingerprints with contributions to both the transient and transient-free zones of FORC diagrams. A fundamental feature of the SV fingerprint is a central ridge, representing a distribution of negative saturation vortex annihilation fields. SV irreversible events at multiple field values along different FORC branches determine the asymmetry in the upper and lower lobes of generic bulk FORC diagrams of natural materials with grains predominantly in the vortex state. Multivortex (MV) FORC signatures are modeled here for the first time. MV grains contribute mostly to the transient-free zone of a FORC diagram, averaging out to create a broad central peak. The intensity of the central peak is higher than that of the lobes, implying that MV particles are more abundant than SV particles in geologic materials with vortex state fingerprints. The abundance of MV particles, as well as their single domain-like properties point to MV grains being the main natural remanent magnetization carriers in geologic materials.

Key Points:
- Micromagnetic modeling of FORC diagrams are key to understanding vortex phenomena in geologic materials
- Single vortex assemblages have both remanent (notably, a central ridge) and transient FORC fingerprints
- Multivortex assemblages are important remanence carriers; their FORC fingerprint is a broad central peak

Supporting Information:
- Supporting Information S1
- Data Set S1
- Data Set S2
- Data Set S3
- Data Set S4

Correspondence to:
I. Lascu,
lascui@si.edu

Citation:
Lascu, I., Einsle, J. F., Ball, M. R., & Harrison, R. J. (2018). The vortex state in geologic materials: A micromagnetic perspective. *Journal of Geophysical Research: Solid Earth*, *123*, 7285–7304. https://doi.org/10.1029/2018JB015909

Received 4 APR 2018
Accepted 20 AUG 2018
Accepted article online 23 AUG 2018
Published online 27 SEP 2018

1. Introduction

Rocks can record information about the geomagnetic field intensity and direction, and preserve it over geologic timescales. Uniformly magnetized, stable single domain (SD) particles are ideal recorders of this information (Néel, 1949), and rock magnetic recording mechanisms are widely tied to their presence in natural materials. For magnetite, SD grains are usually a few tens of nanometers in size in the case of equidimensional particles, and up to 200 nm for elongated particles. Slightly larger particles have nonuniform magnetization states and have been traditionally classified as pseudo single domain (PSD), because of their transitional properties between SD and larger, multidomain (MD) grains. These intermediate-size grains have the capacity to acquire remanent magnetization efficiently, like SD particles, but have lower coercivities, akin to MD particles (Stacey, 1962, 1963). For PSD magnetite, grain size ranges from around 100 nm to a few μm, depending on grain morphology. These particles are not uniformly magnetized but are not partitioned into magnetic domains either. They are mostly found in vortex configurations (e.g., Shcherbakov et al., 1990; Williams & Dunlop, 1995). Since vortex phenomena adequately explain the physics of the magnetization in these particles, Roberts et al. (2017) have proposed replacing the term *PSD state*, which is used purely functionally, with *vortex state*. Roberts et al. (2017) presented evidence for single vortex (SV) processes providing the physical explanation for PSD behavior at the fine end of the grain size range and explored the role of multiple vortices in explaining the physics at the coarse end of the PSD spectrum.

In finite-element micromagnetic calculations, magnetic vortices are the lowest energy states for nonuniformly magnetized particles just above the SD upper threshold (Williams & Dunlop, 1995). Recently, Almeida et al. (2016) and Nagy et al. (2017) have demonstrated that SV particles can have very high blocking temperatures (close to the Curie point for magnetite) and relaxation times larger than the age of the Earth. Calculations have shown that equidimensional SV magnetite grains up to 1,000 nm in size are among the best carriers

of remanent magnetization in natural samples (Nagy et al., 2017). Considering their grain size range, vortex state particles are much more abundant in rocks than SD particles, and they are the main natural remanence carriers in geologic samples. Most rocks do not contain equidimensional SV particles but are still very good paleomagnetic recorders (e.g., Carvallo et al., 2006; Smirnov & Evans, 2015). These rocks will likely contain a combination of SV grains, some with shape anisotropy (Einsle et al., 2016), and larger grains that accommodate multiple vortices and related micromagnetic configurations (Roberts et al., 2017).

Particles in the vortex state grain size range can be reliably identified using first-order reversal curve (FORC) diagrams, which are sensitive to grain size, domain state, and magnetostatic interactions (Pike et al., 1999; Roberts et al., 2000, 2014). The vortex state fingerprint in FORC diagrams is distinct from SD and MD fingerprints, representing an intermediate geometry between the high coercivity horizontally spread distribution of the former and the low coercivity vertically spread distribution the latter (Roberts et al., 2014). Roberts et al. (2017) have reasoned that FORC diagrams should be used as a diagnostic tool for the presence of vortex state particles in natural samples, as they are sensitive to the presence of single vortices. They have also recognized that micromagnetic modeling of particles containing multiple vortices is needed in order to paint a complete picture of the vortex state.

The goal of the present article is to model FORC distributions of SV and multivortex (MV) particles with realistic morphologies (as found in geologic samples), using finite-element micromagnetic modeling. The only micromagnetic simulations of vortex FORC diagrams have been performed by Carvallo et al. (2003), Roberts et al. (2017), and Valdez-Grijalva (2018) who have modeled simple SV grain morphologies. No micromagnetic FORC simulation exists for the MV state. Here we have reconstructed a micrometer-scale volume from an obsidian sample containing magnetite particles up to several micrometers in size and use it as input for a micromagnetic model that simulates experimental FORC acquisition protocols for individual particles. We show that SV and MV micromagnetic configurations control the geometry of FORC signatures observed experimentally and that they account for most of the features observed in samples with particles that span the entire vortex state grain size continuum.

2. Materials and Methods

The specimen investigated in this study is an obsidian fragment from Glass Buttes, Oregon. Geochemically, it can be ascribed to type C/gamma obsidian, based on characteristic ratios of Eu/Th, Rb/Sr, and Zr/Ba (Ambroz et al., 2001; Frahm & Feinberg, 2015). FORC acquisition was performed at the University of Cambridge using a Lake Shore Cryotronics, Inc. PMC-3900 Series vibrating sample magnetometer. Between 193 and 283 FORCs were collected for each experiment, with a measurement resolution of 1–2 mT. FORCs were processed in FORCinel 3.0 (Harrison & Feinberg, 2008), using the VARIFORC variable smoothing algorithm of Egli (2013). Low-temperature magnetization was measured using a Quantum Design Magnetic Properties Measurement System at the University of Cambridge. The sample was cooled in a 2.5 T field from 300 to 20 K, temperature at which the field was switched off and the remanent magnetization measured on warming back to 300 K in 5-K increments. The sample was subsequently cooled in zero field from 300 to 20 K, at which temperature a 2.5 T remanent magnetization was imparted and measured on warming as described above. Magnetic susceptibility was measured in argon as a function of temperature from 25 to 700 °C, and back to room temperature, using an AGICO MFK1 Kappabridge susceptometer at the University of Cambridge.

Three-dimensional reconstruction of a micrometer-scale region of interest (MROI) was accomplished via nanotomography, performed with a FEI Helios Nanolab dual-beam focused ion beam-scanning electron microscope (FIB-SEM) at the Wolfson Electron Microscope Suite, University of Cambridge. FIB-nanotomography (FIB-nT) involves serially milling through the sample using the FIB and imaging each cross section with the SEM (Einsle et al., 2016, and references therein). All FIB milling was performed using an accelerating voltage of 30 kV. The MROI was prepared using ion beam induced deposition (with a 3 nA ion beam current) to lay down a 1-μm-thick tungsten pad. The MROI was isolated from the bulk sample by selectively milling 20-μm-deep trenches on three sides of the region defined by the tungsten pad. The front trench allows full viewing access to the cross-section and the side trenches minimize re-deposition effects associated with the sequential milling process. Three linear fiducial marks were created by milling into the tungsten pad, and then back filling with carbon and capping with tungsten before starting the automated sequence. This was done to minimize the amount of image drift in the SEM image stack (Jones et al., 2014). A second fiducial cross was used to control of the placement of each slice in the tomographic sequence. Each 10-nm-thick tomographic

Table 1
Particle Characterization

Particle ID	Morphology	Volume (μm^3)	DEVS[a](nm)	Domain state[b]	M_{rs}/M_s[c]
gm1	uniaxial	0.00006	24	SD	
gm2	equidimensional	0.012	290	SV	−0.018 (X)*
					0.029 (Y)*
					0.015 (Z)*
					0.006 (D)*
gm3	flattened	0.022	350	MV	0.070 (X)
					0.276 (Y)
					0.287 (Z)
					0.283 (D)
gm4	flattened	0.039	414	MV	0.043 (X)
					0.589 (Y)
					0.394 (Z)
					0.433 (D)
gm5	elongated	0.076	526	MV	0.033 (X)
					0.559 (Y)
					0.446 (Z)

[a]Diameter of equivalent volume sphere. [b]From micromagnetic configuration in zero field: SD = single domain, SV = single vortex, MV = multivortex. [c]Saturation remanence ratio, corresponding to field direction in parentheses
*Values for gm1-gm2 ensemble.

slice was milled away using a 920 pA ion beam current. All milling was performed at 52° stage tilt, which is normal to the FIB. Imaging of the cross-sectional cut face was achieved using backscattered electron imaging with the SEM operating in immersion mode at a low accelerating voltage of 2 kV with a beam current of 86 pA. The resulting three dimensional particle volumes were reconstructed using a modified version of the protocol described by Einsle et al. (2016). After image denoising using a nonlocal means filter, the carbon fiducial marks were used to provide a template based stack alignment. This minimized morphological errors resulting from fiducial free stack alignment. The binary segmentation of the images followed the protocol mentioned above.

A selection of particles spanning the vortex state grain size range were chosen for micromagnetic modeling. Particles were cropped from the segmented FIB-nT stack and converted to tetrahedral finite-element meshes using the software packages Cubit and Iso2Mesh (Fang & Boas, 2009). Tetrahedral nodes were generated at 5- to 10-nm intervals, depending on particle size. Micromagnetic modeling was performed using Micromagnetic Earth Related Rapid Interpreted Language Laboratory (MERRILL), a micromagnetics package optimized for rock magnetism (Ó Conbhuí et al., 2018). MERRILL uses a finite element method/boundary element method to solve for the magnetic scalar potential inside the particle and thereby calculate the demagnetizing energy of the system. Simulations were performed by minimizing the total magnetic energy using a conjugate gradient method, specially adapted to micromagnetic problems. The upper branch of the hysteresis loop was obtained for fields from 300 to −300 mT, in 5-mT decrements. Each point on the upper branch was then used as the initial state for simulating FORC acquisition. Reversal curves were obtained using 5-mT field increments. Micromagnetic FORC simulations were performed on a pair of adjacent grains (gm1 and gm2), respectively in SD and SV states at remanence, as well as on 3 MV particles (gm3, gm4, and gm5; Table 1). Four FORC protocols were simulated for the gm1-gm2 pair, with the field parallel to 3 orthogonal directions (X, Y, and Z), as well as along the diagonal (D) of the reference system. Three FORC protocols were simulated for gm3, with the field parallel to Y, Z, and D. One FORC protocol was simulated for each of the other MV particles, with the field parallel to Z for gm4 and Y for gm5. Simulated FORCs were then imported in FORCinel 3.0 and processed using LOESS smoothing, with a smoothing factor (SF) of 2.5 (Harrison & Feinberg, 2008). Positive and negative features in the FORC diagram result from evaluating the slopes of successive FORC branches (i.e., M_j and M_{j+1}, with $1 \leqslant j \leqslant n-1$; where n is the total number of FORC branches) using the FORC function ρ (e.g., Pike et al., 1999). Features resulting from the evaluation of a pair of successive branches plot along a linear path in the

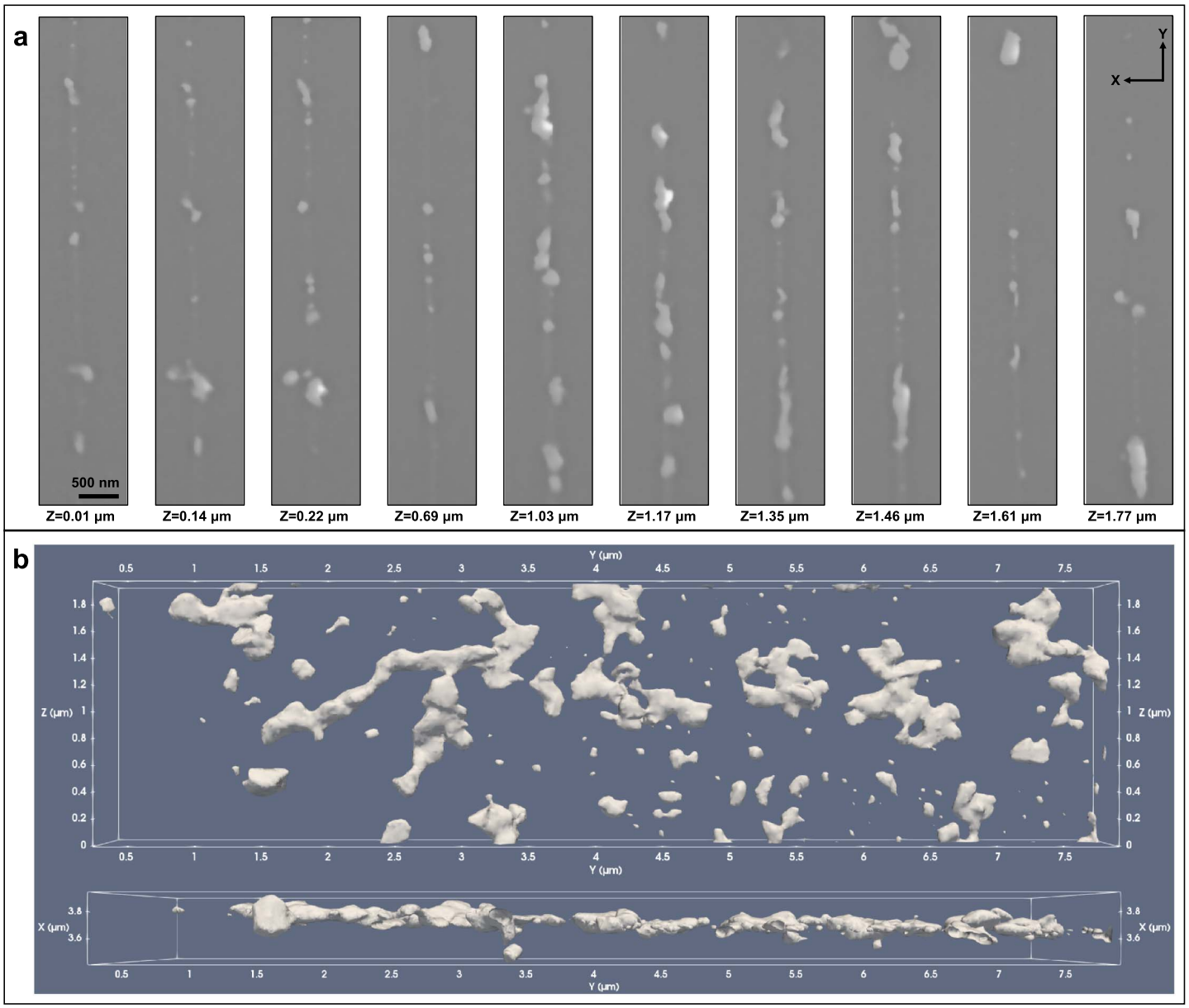

Figure 1. Magnetite layer in Glass Buttes obsidian. (a) Examples of imagery acquired during the FIB slice and view protocol. (b) Two views of the volume reconstructed via FIB-nanotomography. Particle sizes vary from ~100 nm to >1 μm. The larger particles have formed through coalescence of smaller grains from neighboring nucleation sites during crystal growth.

FORC diagram defined by the derivative of the difference FORCs with respect to the measurement field, i.e., $(M_{j+1} - M_j)'$ (Egli & Winklhofer, 2014). Surface meshes and individual micromagnetic states are reproduced here using ParaView (Ahrens et al., 2005).

3. Results

The SEM images and reconstructed volume from FIB-nanotomography show a 300- to 500-nm-thick layer formed of particles with dimensions from tens to hundreds of nm in size and variable morphologies (Figure 1). Whereas smaller grains are mostly equidimensional, larger grains appear to have formed as a result of the coalescence of smaller grains during growth, leading to complex flattened and elongated grain morphologies. Ma et al. (2007) have demonstrated that the Glass Buttes obsidian microstructure consists of many such layers of magnetite nanoparticles, which may be locally folded depending on the dynamics of melt flow.

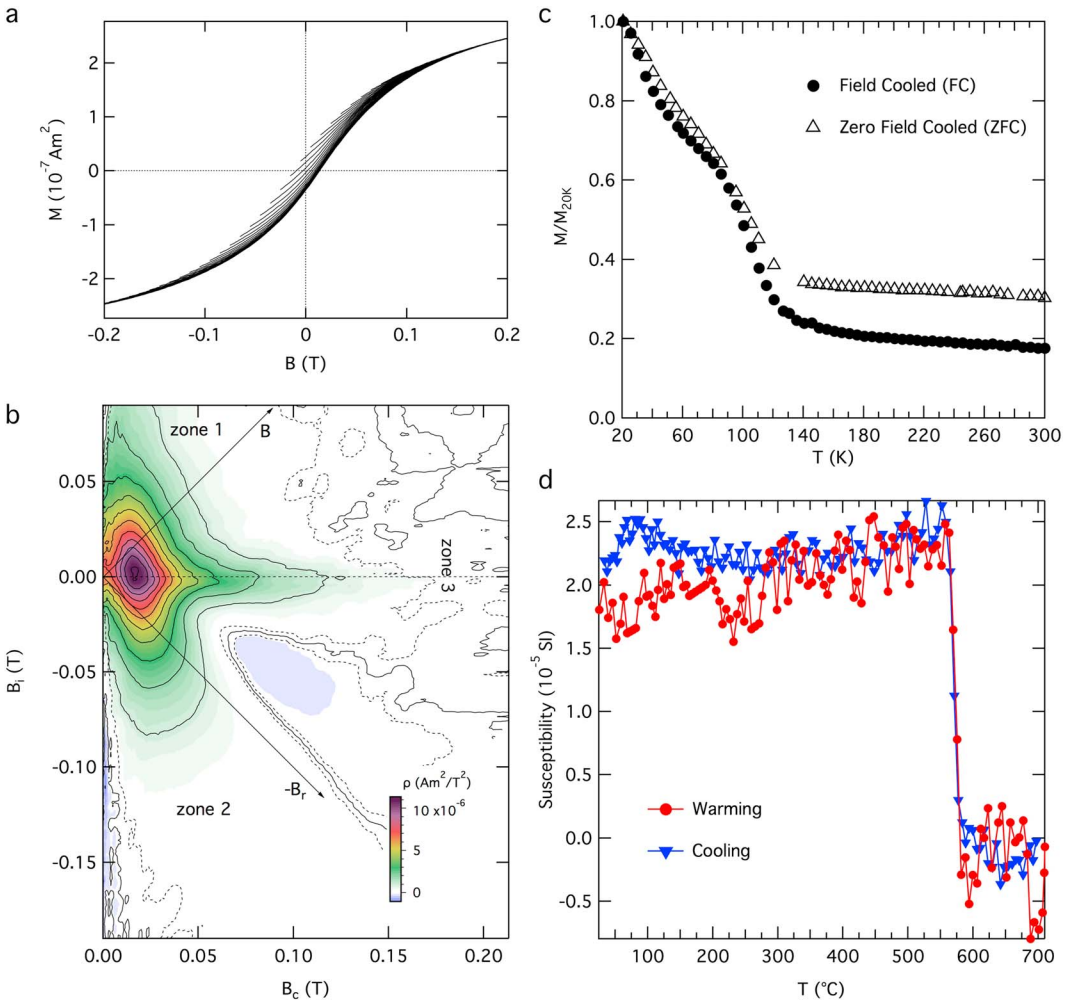

Figure 2. (a) FORC measurements of Glass Buttes obsidian sample. For clarity, only every 5th FORC is plotted. (b) FORC diagram resulting from processing the FORCs in (a) using the following smoothing parameters: $s_{c,0} = s_{b,0} = 9$, $s_{c,1} = s_{b,1} = 9$, $\lambda = 0.2$. Contour interval is 10^{-6} Am^2/T^2. Dashed contour delineates regions of the FORC distribution significant at the 0.05 level (Heslop & Roberts, 2018). See text for description of the component features of the FORC fingerprint and the zones they occupy (labeled 1, 2, and 3). The three zones are delimited by the diagonals of the FORC diagram, which represent the (B, B_r) coordinates. c) Low temperature 2.5 T remanence measured on warming after two different pretreatments: cooling in field (FC) and cooling in zero field (ZFC). d) Magnetic susceptibility as a function of temperature. FORC = first-order reversal curve.

An experimental FORC diagram is shown in Figure 2. The tri-lobate geometry of the FORC signature is typical for the vortex state (Roberts et al., 2014). The upper and lower lobes are not symmetrical with respect to the horizontal axis. The upper lobe contours intersect the vertical axis at higher absolute values than the lower lobe contours, which tend to intersect the vertical axis closer to the origin. The middle lobe is narrower and extends along the horizontal axis but is not centered on it. The lower lobe is flanked by two negative regions, which define the shape of its contours, with the negative area between the lower lobe and middle lobe being more prominent. Where the three lobes come together, there is a broad peak with an intensity a few times larger than that of the lobes. The upper and lower lobes are located in zone 1 ($B > 0$, $B_r > 0$) and zone 2 ($B < 0$, $B_r < 0$) of the FORC diagram, respectively. These zones are associated with transient magnetization events, which only exist in the presence of an external field so will not contribute to the remanent magnetization of the sample (Egli & Winklhofer, 2014; Fabian, 2003; Fabian & von Dobeneck, 1997; Zhao et al., 2002). The middle lobe, the more prominent negative area, and the central peak are located in zone 3 ($B>0$, $B_r<0$) of the FORC diagram, and are associated with transient-free magnetization events, and may contribute to the remanent magnetization of the sample (Egli & Winklhofer, 2014; Fabian, 2003; Fabian & von Dobeneck, 1997; Zhao et al., 2017). Figure 2c shows low temperature magnetization curves exhibiting a Verwey transition (~120 K), which

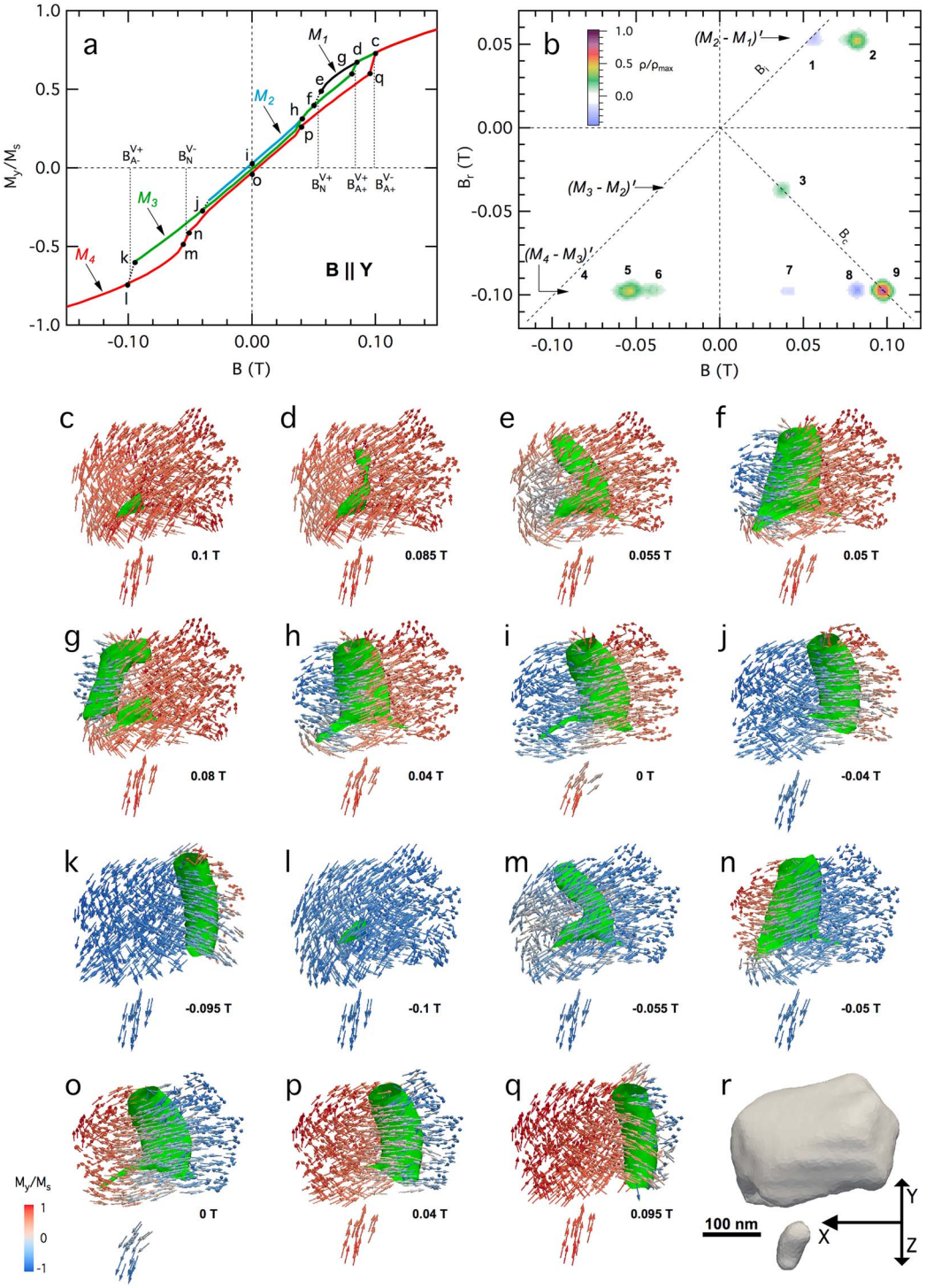

Figure 3. Micromagnetic FORC simulation of the gm1-gm2 ensemble with the field applied along Y. (a) Simulated FORCs: the four branches are labeled M_1 to M_4. Letters indicate panels corresponding to micromagnetic states at positions marked by black dots. B_N is the nucleation field, while B_{A+} and B_{A-} are annihilation fields along ascending and descending branches, respectively. The $V+$ and $V-$ superscripts represent the positive and negative saturation vortices. (b) FORC diagram, processed using simple smoothing, with SF = 2.5. Positive and negative features (labeled 1-9, discussed in text) plot along three horizontal paths, labeled $(M_2 - M_1)'$, $(M_3 - M_2)'$, and $(M_4 - M_3)'$, located at reversal fields (B_r) where magnetization jumps have occurred. The diagonals of the diagram are the B_c and B_i axes. (c–q) Micromagnetic states corresponding to field values labeled in (a). Surfaces (green) delineate vortex cores. (r) Meshes of gm1 and gm2, and their orientation: the Y and Z directions are at 45° to the plane of the figure (i.e., the view is parallel to the diagonal of the (Y,Z) coordinate plane, which points into the figure plane. FORC = first-order reversal curve.

is a diagnostic feature for magnetite. The transition is not sharp, indicating that the magnetite is partially oxidized. The proportion of remanence lost across the Verwey transition is ~20–50% larger for the field cooled curve, which is typical for "PSD" state grains. The susceptibility curves (Figure 2d) exhibit a Curie temperature of ~580°, confirming the main magnetization carrier to be magnetite.

3.1. SV FORC Simulations

To understand each element of the FORC diagram fingerprint and the processes that lead to it, we turn to the micromagnetic models of the particles reconstructed from FIB nanotomography. Even though FORCs were simulated starting at every point on the upper hysteresis branch, only a limited number of discreet FORC branches resulted for each direction. Individual FORC branches are defined at reversal fields (B_r) where an irreversible magnetization event occurs. For the pair of smallest grains (gm1-gm2), there are only a limited number of possible features in the FORC diagram. To understand the origin of these features, we examine the FORC diagram simulated with the field along Y, as it resulted in only four distinct FORC branches, and it exhibited the simplest FORC diagram signature (Figure 3). The FORC branches are labeled M_1 to M_4 in Figure 3a. The FORC function, plotted in (B, B_r) space (Figure 3b), exhibits nonzero features along three horizontal paths, corresponding to reversal field values where magnetization jumps have occurred. These paths are labeled $(M_2 - M_1)'$, $(M_3 - M_2)'$, and $(M_4 - M_3)'$ in Figure 3b.

Both particles (Figure 3r) are in SD states at saturation. As the field (B) is decreased from positive saturation along M_1, the larger particle transitions from a flower to a curling configuration via coherent moment rotation. By 0.1 T a proto-vortex core starts forming (Figure 3c) and continues to gradually develop by the same rotation mechanism to the field value of 0.055 T (Figure 3e). Up to this point the magnetization changes are reversible, and all the FORCs have identical paths to M_1. The first irreversible transition occurs between 0.055 and 0.05 T, with the vortex fully nucleating (Figure 3f), that is, occupying a local energy minimum. Subsequent FORCs follow branch M_2 from 0.05 up to 0.085 T (points f and d in Figure 3a). On this segment, the vortex core translates in the +X direction and denucleates at the magnetization jump between 0.08 T (Figure 3g) and 0.085 T (Figure 3d).

The difference in the rate of magnetization change along branches M_2 and to M_1 is evaluated using the FORC function (Figure 3b). The corresponding contribution of this difference plots along the horizontal path between $B_r = 0.055$ and 0.05 T, and consists of two features, one negative (labeled 1) and one positive (labeled 2), which are proportional to $(M_2 - M_1)'$. Feature 1 results from the difference in the slopes of M_2 and M_1 between $B = 0.055$ and 0.06 T, and is negative because the slope of M_1 is greater than the slope of M_2 on this segment. Feature 2 is a point peak, and is the result of the irreversible magnetization change associated with the annihilation of the positive saturation vortex (V^+). This creates a contribution proportional to the Dirac delta function accounting for the irreversible event, which has an amplitude equal to the magnetization jump (Egli & Winklhofer, 2014). Peak 2 is positive because the jump occurs on M_2 (i.e., the branch starting from a lower reversal field).

All FORCs starting at reversal fields between 0.05 and −0.035 T coincide with M_2. As the field is decreased along the upper hysteresis branch, the vortex core progressively translates in the −X direction (Figures 3f–j), while the SD particle moments begin to curl (see 0 T configuration, Figure 3i). The next magnetization jump occurs between −0.035 and −0.04 T (Figure 3j), at the switching field of the SD particle. Subsequent FORCs follow M_3, which runs mostly parallel to M_2 up to 0.035 T and then merges with it at the SD switching field (Figure 3h). This jump on M_3, coupled with no change in the slope of M_2 between $B = 0.035$ and 0.04 T results in a positive point peak (labeled 3 in Figure 3b) in the FORC diagram between $B_r = 0.035$ and 0.04 T, along path $(M_3 - M_2)'$.

Decreasing the field along the upper hysteresis branch from −0.04 to −0.095 T (Figure 3k), the vortex core continues to translate in the −X direction. The last FORC branch (M_4) is accessed between −0.095 and −0.1 T (Figure 3l), as V^+ is finally annihilated, on side of the grain opposite to that on which it nucleated. M_4 coincides with the lower hysteresis branch, and all micromagnetic states and events will mirror those associated with the upper hysteresis branch. The negative saturation vortex (V^-) develops gradually between −0.1 and −0.055 T (Figure 3m), with the vortex core fully nucleating at the irreversible jump to −0.05 T (Figure 3n). V^- has the same geometry and sense (right-handed) as its positive saturation counterpart. The difference is in the orientation of spins, which are flipped, giving rise to a vortex configuration with equal net moment and opposite polarity. With progressively increasing fields, the vortex core is being driven out in the −X direction,

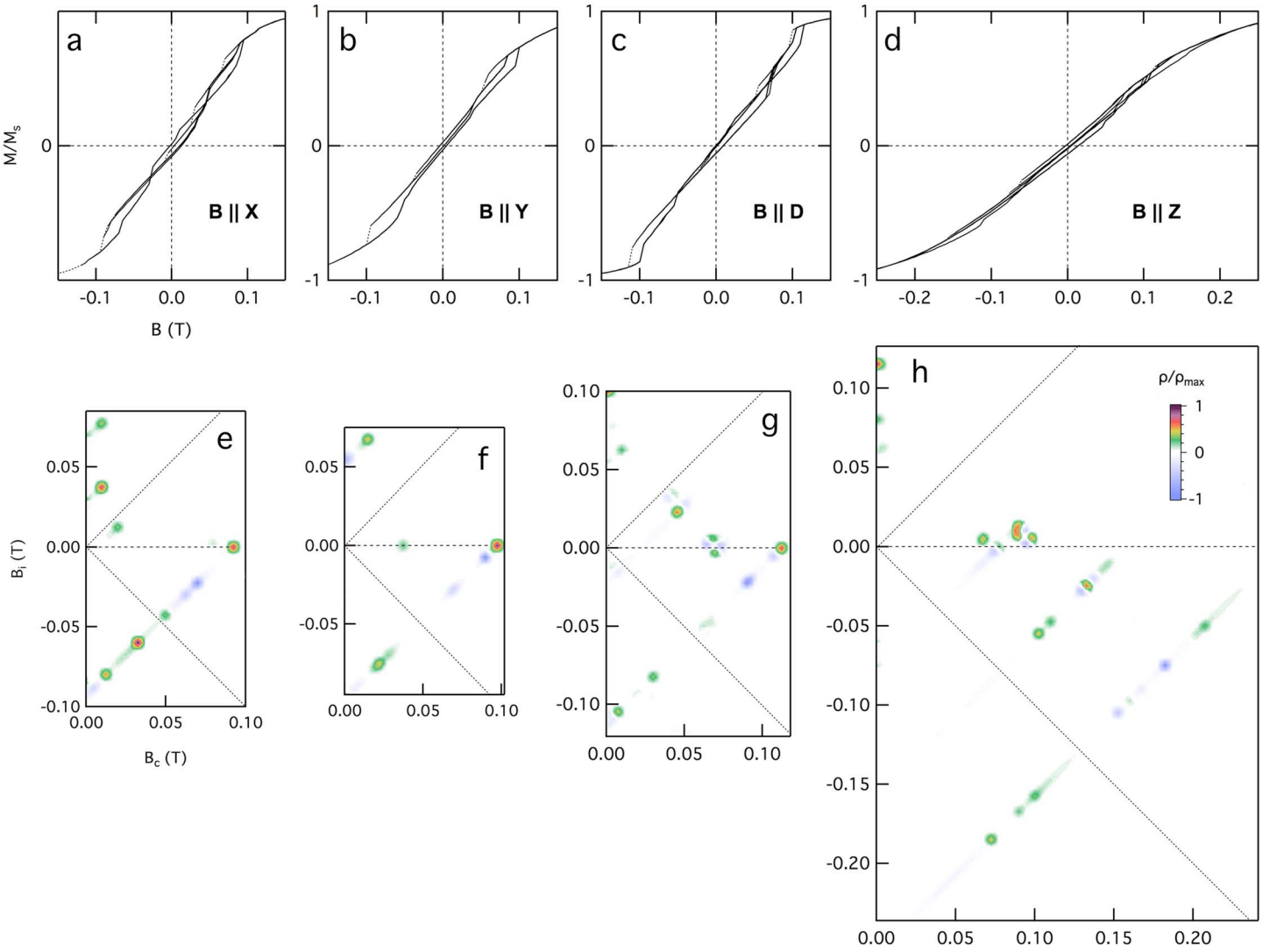

Figure 4. Simulated FORCs (a–d) and FORC diagrams (e–h) of the gm1-gm2 ensemble along four field directions: X (a, e), Y (b, f), Z (c, g), and D (d, h). Direction D is the diagonal of the coordinate system plotted in Figure 3. SF = 2.5. FORC = first-order reversal curve.

the same as for the upper branch. Switching of the SD particle occurs between 0.035 and 0.04 T (Figure 3p). Finally, V^- is annihilated between 0.095 T (Figure 3q) and 0.1 T (Figure 3c).

Most of the features of the FORC diagram (labeled 4–9) are along path $(M_4 - M_3)'$, between $B_r = -0.095$ and -0.1 T, representing the evaluation of M_4 against M_3 (Figure 3b). Features 4 and 6 are caused by differences in the slopes of the FORCs. Between $B = -0.095$ and -0.075 the slope of M_3 is greater, giving rise to feature 4, whereas between -0.045 and -0.035 the slope of M_4 is greater, giving rise to feature 6. The rest of the features are point peaks involving magnetization jumps. Peaks 5 and 9 are positive, as the jumps (caused by V^- nucleating and annihilating, respectively) occur on M_4. Peak 8 is negative because the jump (caused by the annihilation of V^+) occurs on the previous branch (M_3). Peak 7 involves magnetization jumps (caused by the SD particle switching) on both FORCs, but the amplitude of the jump on M_3 is greater than that of the jump on M_4, so the peak is negative. In addition, peak 7 is flanked by negative trails caused by the greater slope of M_3 on both sides of the SD switching event.

To summarize the distribution of the features in the FORC diagram, features 1 and 2 plot in zone 1; peaks 4, 5, and 6 in zone 2; and peaks 3, 7, 8, and 9 in zone 3 of the FORC diagram (Figure 3b). In zone 3, peak 3 and peak 9 contribute to the central ridge of the FORC diagram (Figure 4f). Most of these peaks are related to SV

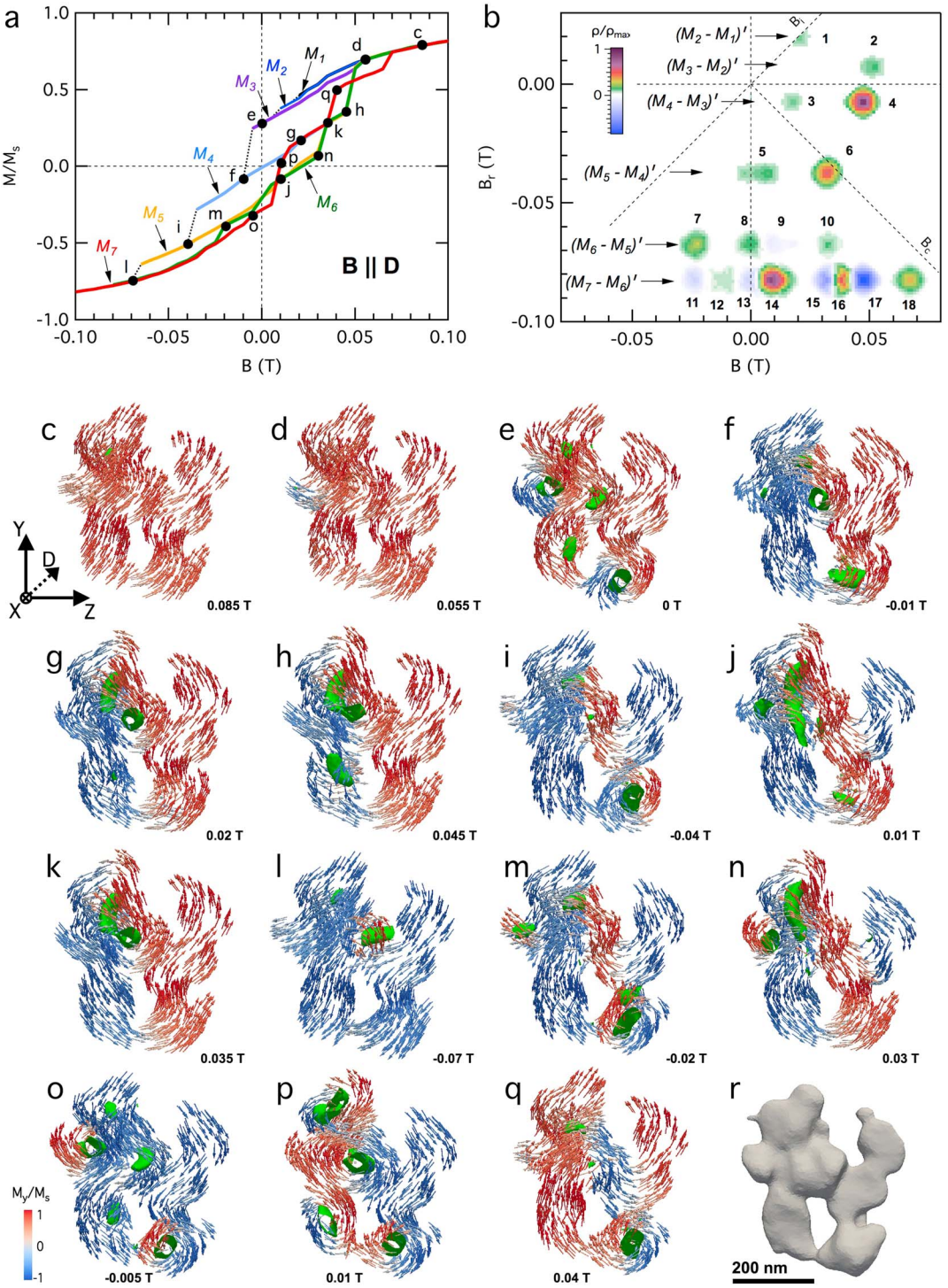

Figure 5. Micromagnetic FORC simulation of particle gm3 with the field applied along D. (a) Simulated FORCs: the 7 branches are labeled M_1 to M_7. Letters indicate panels corresponding to micromagnetic states at positions marked by black dots. (b) FORC diagram, processed using simple smoothing, with SF = 2.5. Positive and negative features (labeled 1–18, discussed in text) plot along 6 horizontal paths (labeled $(M_{j+1} - M_j)'$, $1 \leqslant j \leqslant 6$) located at reversal fields (B_r) where magnetization jumps have occurred. The diagonals of the diagram are the B_c and B_i axes. (c–q) Micromagnetic states corresponding to field values labeled in (a). Surfaces (green) delineate vortex cores. (r) Mesh of particle gm3. The view is parallel to X, which points into the figure plane. FORC = first-order reversal curve.

irreversible magnetization events, except for Peak 3, which is due to SD switching, and peak 7, which is a result of the interplay of SV and SD magnetization phenomena.

The FORC diagrams obtained by applying the field along X ($FORC_X$), Z ($FORC_Z$), and D ($FORC_D$) are slightly more complex but are also characterized by only a finite number of positive and negative features that contribute to all three zones of the FORC diagrams (Figure 4). In all three field directions some of the FORC branches intersect, protruding into (B, M) space that is not accessible to the major hysteresis loop (Figures 4a, 4c, and 4d). Similar to $FORC_Y$ (Figure 4f), the annihilation of V^- along the lower branch contributes a strong positive peak to the central ridge of $FORC_X$ and $FORC_D$ (Figures 4e and 4g). Due to shape anisotropy, $FORC_Z$ is in a magnetically hard direction, and the resulting FORC diagram is spread out to high field values (Figure 4h). In addition, we observe a number of peaks that cluster around the horizontal axis, representing vortex denucleation fields that do not contribute to the central ridge. With the field applied along X, gm1 interacts with gm2 such that SD switching contributes a peak with a coercivity between 0.075 and 0.08 T that is displaced upward from the horizontal axis (Figure 4e). With the field applied along Z and D, gm1 does not interact with gm2, and switches respectively between 0.075 and 0.08 T (Figure 4h), and 0.11 and 0.115 T (Figure 4g), contributing to the central ridge.

3.2. MV FORC Simulations

We investigate the FORC fingerprint of MV particles by focusing on the FORC diagram of particle gm3 (Table 1), with the field applied along D (Figure 5). There are 7 FORC branches, labeled M_1 to M_7 in Figure 5a, which yield the main features in the FORC diagram (Figure 5b). The particle (Figure 5r) is uniformly magnetized at saturation. As the field is decreased, the moments start relaxing into local curling configurations (Figures 5c and 5d) that will serve as nucleation spots for multiple vortex structures. Figure 5e shows the particle at saturation remanence with five vortex nucleation sites, two of which are fully nucleated (lower-right and left sides of the particle) as a result of the irreversible magnetization events at the reversal fields corresponding to the beginning of FORC branches M_2 and M_3. In the FORC diagram (Figure 5b), differences in the slopes of M_1 and M_2, and of M_2 and M_3 produce two positive features in zone 1, respectively along $(M_2 - M_1)'$ between 0.015 and 0.02 T (peak 1), and along $(M_3 - M_2)'$ between 0.05 and 0.055 T (peak 2).

The largest irreversible magnetization change on the upper hysteresis branch occurs between −0.005 and −0.01 T (Figure 5a), as the vortices in the center and upper part of the particle nucleate, while the other three are either annihilated or in the process of denucleation (e.g., lower right vortex is being driven out in the −Z direction; Figure 5f). With increasing field along branch M_4, the two central vortices start to merge between 0.015 and 0.02 T, with another vortex core starting to nucleate below it on the left side of the particle, while the vortex on the lower right is annihilated (Figure 5g). Merging of the cores of the two central vortices is complete by 0.045 T (Figure 5h), with the resulting structure being annihilated between 0.045 and 0.055 T (Figure 5d) in two field steps, the first one being the most prominent jump. In the FORC diagram, the evolution of these multiple vortices is captured via two positive peaks along $(M_4 - M_3)'$, marking the jump at 0.02 T (peak 3) that results in a configuration with 3 vortex cores on the left side of the particle (see Figure 5g), and the annihilation of the vortices at the large magnetization jump between $B = 0.045$ and 0.05 T (peak 4).

The next FORC branch, M_5, is accessed at the jump between −0.035 and −0.04 T. The micromagnetic configuration at the reversal field (Figure 5i) shows the two central vortices denucleating, and the moments in the upper right side of the particle flipped (now pointing in the −Y direction). The vortex core in the lower right is shifted in the +Z direction, and now parallel to X (*cf.* with Figure 5f). With increasing field along M_5, this vortex is being driven out in the −Z direction, while a large central vortex with an elongated, winding core forms as a result of the merger of the previous central vortex cores at a jump between 0.005 and 0.01 T (Figure 5j). The next irreversible event occurs at 0.035 T (Figure 5k), when the moments in the upper right part of the particle switch, the central vortex structure ends up in the same local energy minimum as on the previous FORC (see Figure 5h), and the lower-right vortex is annihilated. After the jump, the paths of M_5 and M_4 coincide. In the FORC diagram there are two positive features (labeled 5 and 6) along $(M_5 - M_4)'$. Feature 5 is a double peak associated with the steepening of the slope of M_5 between −0.005 and 0.01 T, coupled with no change in the slope of M_4. Peak 6 occurs between 0.03 and 0.035 T and marks the merging of the two FORC branches.

As the field is decreased from −0.04 T along the upper hysteresis branch, the vortex in the lower right is annihilated between −0.065 and −0.07 T via core translation in the +Z direction, while a vortex nucleates in the center of the particle, with its core oriented along Z (Figure 5l). A core nucleation site also begins to develop in upper left part of the grain. This micromagnetic state corresponds to the first point on branch M_6.

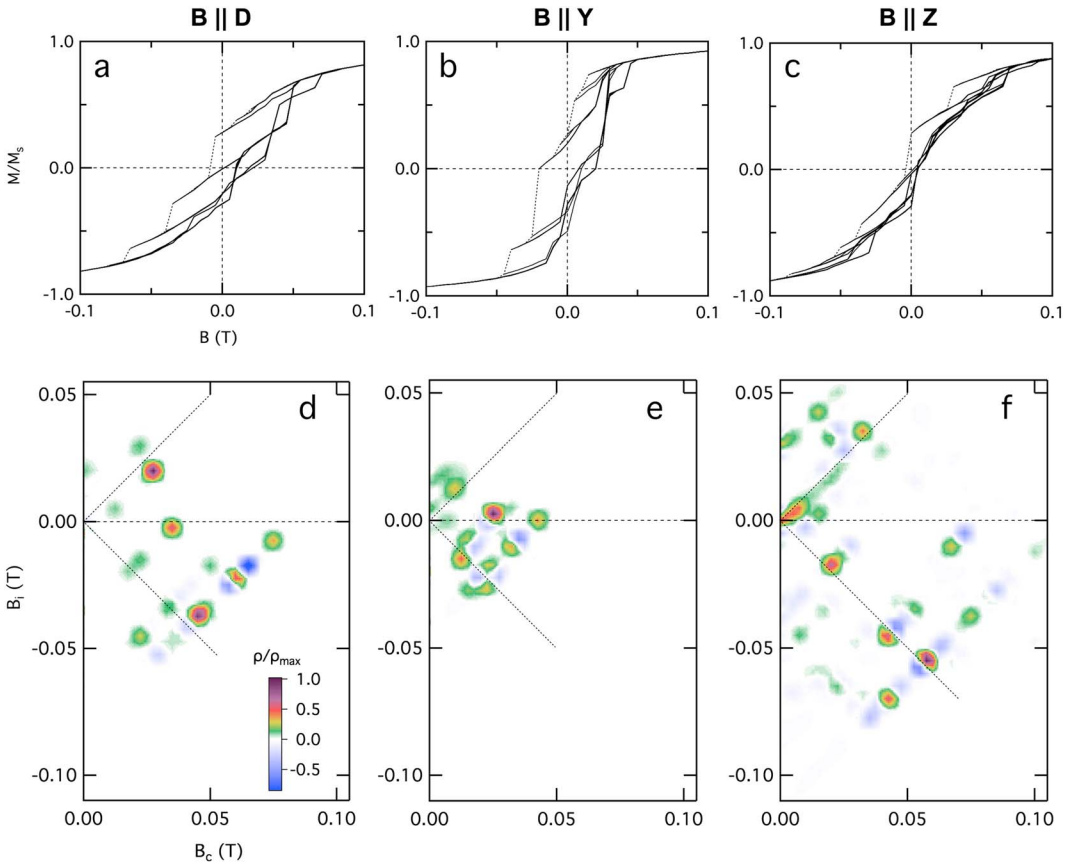

Figure 6. Simulated FORCs (a–c) and FORC diagrams (d–f) of particle gm3 along three field directions: D (a, d), Y (b, e), and Z (c, f). Direction D is the diagonal of the coordinate system, as seen in Figure 5. SF = 2.5. FORC = first-order reversal curve.

Along M_6, the first jump occurs between −0.025 and −0.02 T, field at which the central core is annihilated and a double vortex nucleates in the lower right of the particle (Figure 5m). The upper left vortex structure continues to develop, and an additional nucleation site appears in the farthest left. The vortex on the left fully nucleates between −0.005 and 0 T. At 0.005 T the upper left vortex fully nucleates with an elongated core oriented parallel to Y, while the lower right double vortex is annihilated . This micromagnetic configuration is very similar to the one presented in Figure 5j, and evolves slightly until 0.03 T (Figure 5n), which is right before the jump between 0.03 and 0.035 T that marks the merger of M_6 with M_5 . In the FORC diagram (Figure 5b) the events occurring on M_6 are evaluated against to the ones occurring on M_5 along the path $(M_6 - M_5)'$. Peak 7 is due to the jump on M_6 that results in the micromagnetic state at −0.02 T (Figure 5m), coupled with no irreversible change on M_5. Between −0.005 and 0.035 T, the positive-negative-positive sequence (peaks 8–10) is due to the difference in the slopes of M_6 and M_5, as follows: between −0.005 and 0.005 M_6 is steeper, but due to the jump on M_5 at 0.01 T the latter becomes steeper up to 0.02 T, giving peaks 8 and 9, respectively. Between 0.02 and 0.03 T, M_5 and M_6 are parallel, with no corresponding signal in the FORC diagram ($\rho = 0$). Peak 10 is a result of the jump between 0.03 and 0.035 T, which has a slightly larger magnitude on M_6 compared to M_5.

M_7 is accessed between −0.08 and −0.085 T, at the last irreversible event along the major hysteresis loop, marking the annihilation of the central vortex (see Figure 5l) and the transition of the particle into a flower state. From the reversal point, as the field is increased along M_7, the same 5 nucleation sites encountered on the upper hysteresis branch will start nucleating vortex structures. From −0.085 to −0.005 T there are two main jumps that result in two vortices forming (Figure 5o): one between −0.035 and −0.03 T (left side) and the other between −0.01 and −0.005 T (lower right). The other three nucleation sites in Figure 5o contain proto-cores due to the incipient curling of the moments around those sites, but the vortices are not fully nucleated, as the rotation of the moments is reversible. The largest irreversible magnetization change occurs between 0.005 and 0.01 T. The micromagnetic state at 0.01 T (Figure 5p) shows that the other three vortices

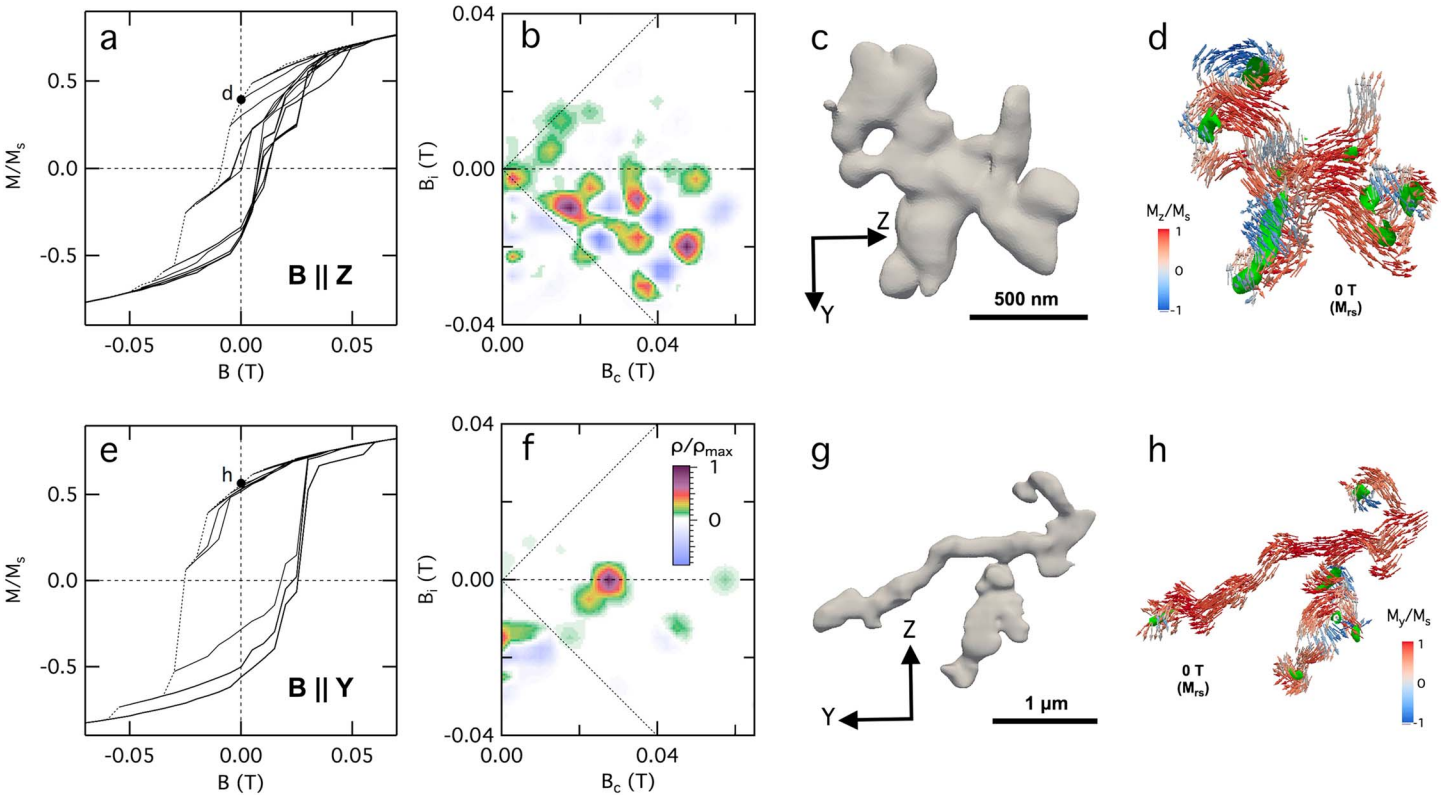

Figure 7. FORC simulations of particles gm4 (a–d, field applied along Z) and gm5 (e–h, field applied along Y): FORCs (a, e), FORC diagrams (b, f), particle meshes (c, g), and micromagnetic states at saturation remanent magnetization, M_{rs} (d, h). SF = 2.5. FORC = first-order reversal curve.

have fully nucleated, while the leftmost vortex has been annihilated. There is an additional jump of smaller magnitude between 0.01 and 0.15 T, in which the left side vortices are annihilated, as the moments on this side of the particle that were not oriented in the +Y direction (blue in Figure 5p) switch. Between 0.015 and 0.035 T, the two remaining vortices (center and lower right) are being driven out, with the central vortex denucleating at the irreversible event occurring between 0.035 and 0.04 T (Figure 5q). Also contributing to this jump is the collective switching of moments in the upper right of the particle (red in Figure 5q). The lower right vortex is annihilated between 0.065 and 0.07 T, producing the last significant jump along M_7. The nucleation of a central vortex with a core parallel to Z and of opposite polarity to its negative counterpart (Figure 5l) also contributes to the magnitude of this event. This vortex is annihilated between 0.08 and 0.085 T (Figure 5c).

The succession of events occurring on M_7 compared to the ones on M_6 plot at the bottom of the FORC diagram along the path $(M_7 - M_6)'$. (Figure 5b). The alternation of negative and positive peaks is due to the frequent changes in the slopes of the two reversal curves, which creates the interweaved pattern (see Figure 5a). The first two negative peaks (11 and 13) are due to the jumps on M_6 occurring between −0.025 and −0.02 T, and between −0.005 and 0.005 T. The peaks flank a positive feature (12), which is a double peak configuration due to the slope of M_7 being steeper between −0.02 and −0.015 T, and between −0.01 and −0.005 T. The most intense positive feature is another double peak (14), caused by the sequence of irreversible changes occurring between 0.005 and 0.015 T along M_7, coupled with no change in slope observed along M_6. The jump between 0.03 and 0.035 T along M_6 , coupled with the jump between 0.035 and 0.04 T along M_7 translates as a pair of negative (peak 15) and positive (peak 16) features, respectively. The intense negative feature between 0.045 and 0.055 T (double peak 17) is due to the large two-step irreversible magnetization change along M_6, couple with no slope change along M_7. Finally, the last major jump along M_7, coupled with no change in the slope of M_6, gives point peak 18 between 0.065 and 0.07 T. The majority of the peaks in the FORC diagram (including the highest intensity ones) plot in zone 3 (Figure 5b), with approximately a third of the features plotting in zones 1 and 2.

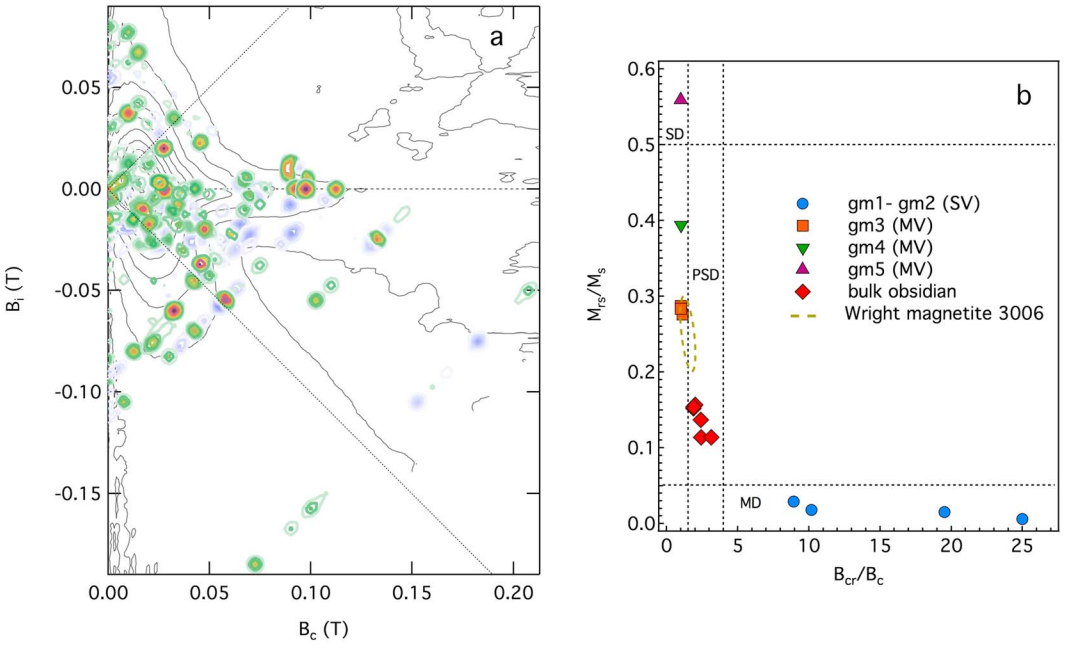

Figure 8. (a) Positive and negative features from the all the FORC diagrams simulated in this study superimposed onto the contours of the experimental FORC diagram shown in Figure 2. (b) Day diagram of the nine simulations and six obsidian samples. Dashed ellipse indicates the range of values for Wright Co. magnetite 3006 (mean grain size 1 μm) hysteresis parameters (Carter-Stiglitz et al., 2001; Dunlop & Carter-Stiglitz, 2006; Harrison et al., 2014; Yu, 2008). FORC = first-order reversal curve.

Two additional FORC protocols were simulated by applying the field along Y and Z (Figure 6). $FORC_Y$ saturates around 0.05 T (Figure 6b), so it has the most restricted range of the three FORC diagrams (Figure 6e). As with $FORC_D$ (Figure 6d), most of the features associated with the evolution of multiple vortex structures plot in zone 3 of the FORC diagram (Figure 6e). $FORC_Z$ saturates > 0.1 T and has a wasp-waisted appearance (Figure 6c). The FORC diagram exhibits a more extensive fingerprint, with peaks distributed in all three zones (Figure 6f). Compared to $FORC_D$ and $FORC_Y$, there are more features in the zones 1 and 2 of the $FORC_Z$ diagram, which explains the wasp-waisted character of the major loop.

MV FORCs were also simulated for two larger particles, gm4 and gm5 (Table 1). The large size of the finite element meshes for these particles made the simulations computationally intensive, which did not permit the generation of more than one FORC protocol for each particle. For gm4 (Figure 7c), the FORCs were simulated with the field along Z (Figures 7a and 7b), while for gm5 (Figure 7g), with the field along Y (Figures 7e and 7f). The micromagnetic states of the particles at saturation remanence are shown in Figures 7d and 7h. Both particles are characterized by multiple vortex cores, as well as regions of uniform magnetization. Almost all of the positive and negative features in the FORC diagram for particle gm4 are contained in zone 3, with minor contributions to the central ridge. Most of the features in the FORC diagram of gm5 are also located in zone 3, the main feature being a very intense positive peak contributing to the central ridge. This peak is due to shape anisotropy-dictated SD-like switching of the moments in the part of the grain with elongated morphology, between 0.025 and 0.03 T. A second, less intense peak contributes to the central ridge between 0.055 and 0.6 T and is due to the SV-like annihilation of the negative saturation vortex located in the upper left of the particle, which does not interact with other vortices.

4. Discussion: The Vortex State in Geologic Materials

Roberts et al. (2017) have proposed that *vortex state* should replace the term *PSD state* in the rock and mineral magnetism nomenclature, because the former provides a meaningful description of the relevant physics of the dominant magnetization process occurring in this transitional domain state. SV nucleation and annihilation processes are fairly well understood and describe the magnetic phenomena observed at the fine end of the vortex state spectrum. MV-related processes, which account for the magnetic phenomena occurring at the coarse end of the vortex spectrum, have been explored to a lesser degree. The micromagnetic simula-

tions presented here from single particles of different sizes and shapes spanning the SV-MV spectrum offer insight into the processes operating in the magnetic vortex state, and unify the signatures observed in FORC diagrams of materials ranging from metallic nanodot arrays (Dumas et al., 2009, 2012; Dumas, Li, et al., 2007; Dumas, Liu, et al., 2007; Pike & Fernandez, 1999; Winklhofer et al., 2008) to SV-rich materials (Lappe et al., 2011, 2013; Zhao et al., 2017) to PSD-dominated bulk rock samples, such as the obsidian from Glass Buttes.

Below, we synthesize our current understanding of the magnetic vortex state, through the lens of FORC diagrams. To illustrate how a handful of FORC diagrams, obtained from four vortex state particles in a limited number of field directions, can map the main features of the FORC diagram of the bulk specimen from which they were extracted, we overlay all the simulated FORC diagrams onto the experimental FORC diagram of the Glass Buttes obsidian (Figure 8). The individual features concentrate in a number of regions of the FORC space: Positive SV peaks plot onto the upper, lower, and middle lobes; negative SV peaks mostly cluster in the negative area between the lower lobe and the middle lobe; MV peaks map onto the central peak. A mix of positive and negative features is expected throughout the FORC space, with the contribution from the positive peaks outweighing that from the negative peaks in the lobes and central peak, and vice-versa for the main negative area of the FORC diagram. This can be readily seen in the relatively unsmoothed version of the experimental FORC diagram (Figure S1 in the supporting information). In the main negative area (Figure 8a) the simulated peaks are scarce, due to the limited number of orientations and particles modeled, but there is a concentration of negative features at the zero contour apex, as well as a number of negative peaks in the region where the contour opens out. Between these two areas are three positive peaks, two of them from the simulation of gm1-gm2 along the hard axis ($FORC_Z$). Given the lack of data in this region, it is not possible to evaluate the agreement with the experimental data. However, in the positive areas, where the data density is higher, the congruence is more than evident. In the lobes and central peak areas there is also a mix of positive and negative peaks, but with a clear preponderance of positive features. This is in excellent agreement with the experimental data.

4.1. SV Phenomena and Their Fingerprint

SV features contribute to zones 1, 2, and 3 of the FORC diagram. SV features in zone 1 are mostly positive peaks associated with the annihilation of the positive saturation vortex (V^+) along intermediate FORCs (e.g., branch M_2 in Figure 3a). When V^+ nucleates after a steep decline in magnetization due to the reversible increase in the degree of curl, as shown in Figure 3, the upper hysteresis branch is curved before the magnetization jump, and has a higher slope than the FORC branch, leading to a negative peak next to the vertical axis of the FORC diagram, preceding the positive peak. The coercivity of the positive peak is $(B_{A+}^{V+} - B_N^{V+})/2$, where B_N^{V+} is the nucleation field of V^+, and B_{A+}^{V+} is the annihilation field of V^+ along the reversal curve (i.e., with the field increasing). If the nucleation occurs after a modest decline in magnetization, so that the FORC branch has a higher slope than the upper hysteresis branch, there is no negative peak, and the positive peak will be located next to the axis. Since the contours of the upper lobe do not close near the origin, the positive contributions must outweigh the negative ones in zone 1, which means that vortex nucleation occurs preponderantly without a precursor proto-vortex curling state.

In zone 2, the coercivity of SV positive peaks is given by $(B_N^{V-} - B_{A-}^{V+})/2$, where B_N^{V-} is the nucleation field of the negative saturation vortex (V^-), and B_{A-}^{V+} is the annihilation field of V^+ along the upper hysteresis branch (i.e., with the field decreasing). This coercivity is higher than for the positive peak in zone 1 because $|B_{A+}^{V+}| < |B_{A-}^{V+}|$. The positive peaks are generally preceded by negative features (see Figures 4e–4h), which occur because the rate of magnetization change along the lower FORC branch is generally lower than along the preceding FORC around B_{A-}^{V+}. The higher coercivities create the asymmetry between the upper and lower lobes, while the presence of negative peaks cause the contours of the lower lobe to close near the origin. This configuration has also been observed in FORC diagrams of materials dominated by SV particles with a broad grain size distribution spanning hundreds of nm and/or heterogeneous morphologies, such as dusty olivine (Lappe et al., 2011, 2013) or hexagonal bacterial platelets Zhao et al. (2017)).

The main contributions to the upper and lower lobes come from transient irreversible events. The two lobes are not restricted to zones 1 and 2. If the nucleation of the positive (negative) saturation vortex occurs in negative (positive) field, then the pair positive peaks contributing to the lobes will plot instead in zone 3 of the FORC diagram and will contribute to remanent magnetization. The lobes can be symmetrical if $B_{A+}^{V+} = B_{A+}^{V-}$, where B_{A+}^{V-} is the annihilation field of V^- along the lower branch. However, this happens only in very specific

circumstances (see Figure 3d of Dumas et al. (2009), and discussion below of magnetic disk oriented parallel to the field) and is unlikely to occur in geologic materials.

In zone 3, noninteracting SV particles contribute a positive peak to the central ridge. Its coercivity is given by $(B^{V-}_{A+} - B^{V+}_{A-})/2$. Since for noninteracting SV particles $B^{V-}_{A+} = |B^{V+}_{A-}|$, the coercivity of this peak will be equal to B^{V-}_{A+}. This is known as inversion symmetry (Egli & Winklhofer, 2014). In natural materials, grain size distributions are sufficiently broad, so that FORCs do not intersect each other (i.e., $B^{V+}_{A+} < B^{V-}_{A+}$). This results in the central ridge peak being preceded by a negative peak with a coercivity of $(B^{V-}_{A+} + B^{V+}_{A+})/2$. The pairing of these two negative and positive features occurs because of the difference in annihilation field values for V^+ and V^-. This difference is due to the vortices annihilating on opposite sides of the particle (compare Figures 3g and 3q). We thus now have the micromagnetic confirmation of the phenomenological model proposed by Pike and Fernandez (1999) for these features. For weakly interacting ensembles of natural SV particles with random packing, these pairs of positive and negative peaks from individual grains will produce a positive ridge along B_c, accompanied by a negative trough below it (Lappe et al., 2011, 2013; Zhao et al., 2017). Our modeling results, together with observations from such natural SV-dominated materials, lead to the conclusion that a central ridge is a fundamental feature of the SV FORC fingerprint. A SV central ridge is distinct from a SD central ridge in three ways: (1) It has a higher median coercivity, because the field necessary to reverse a vortex is higher than the field required to switch a SD particle or chain of particles; (2) it has approximately the same intensity as the upper and lower lobes, whereas the intensity of a SD ridge is an order of magnitude higher than other contributions; and (3) it is adjacent to a negative trough below it, as opposed to a positive area above the lower diagonal in the SD case. Our obsidian exhibits a central lobe, not a ridge, and a broader, weakly negative area closer to the lower diagonal, rather than a trough next to B_c, so there must be significant inter-particle magnetostatic interactions that are broadening the ridge and negative trough, and shifting its center below the horizontal axis. The advent of variable smoothing has already allowed the identification of central ridges in natural samples with vortex FORC fingerprints (Egli, 2013; Ludwig et al., 2013)

If $B^{V+}_{A+} > B^{V-}_{A+}$, the lower branch intersects the preceding FORC branch, which causes the negative peak to occur after the central ridge peak (i.e., plots above the B_c axis). This occurs only in specific circumstances, such as for materials with very narrow SV particle size distributions and planar arrangements (e.g., thin films of metallic nanodots). In these materials, some of the lower FORC branches intersect the FORCs of the half loop ($B > 0$) for particular field orientations (Dumas, Li, et al., 2007; Dumas, Liu, et al., 2007; Dumas et al., 2009, 2012; Pike & Fernandez, 1999; Winklhofer et al., 2008). This creates a negative trough above the central ridge, which generally has a lower intensity than the trough below the central ridge. Finally, the rare situation in which there is no SV contribution to the central ridge occurs only if $B^{V+}_{A+} = B^{V-}_{A+}$, which also results in symmetrical positive contributions to zones 1 and 2, as noted above.

Prior to micromagnetic modeling efforts, SV features in FORC diagrams have been explained using a combined experimental and theoretical approach. In measuring SV metallic nanodots with narrow particle size distributions and planar arrangements, various authors have observed the following features in FORC diagrams: two broad, elliptical positive peaks in both half planes of the FORC diagram; a negative area next to the B_i axis in zone 2; and a high coercivity central ridge paired with a negative trough below it, and in some cases a second negative trough above it (Dumas, Li, et al., 2007; Dumas, Liu, et al., 2007; Dumas et al., 2009, 2012; Pike & Fernandez, 1999; Winklhofer et al., 2008).

A further step was taken when the first finite-element micromagnetic simulations of SV FORC diagrams were produced. Carvallo et al. (2003) modeled a 100 ×80× 80 nm magnetite parallelepiped, which produced FORCs that follow five main branches. These branches exhibit random splitting into different subbranches around the field values at which irreversible events occur. This happens when the solution to the minimization algorithm in the micromagnetic model does not reach equilibrium. The presence of "hooks" at the beginning of many of the reversal curves also supports the premise that these solutions may have routinely not reached equilibrium. We have observed in our models that the number of iterations needed for convergence often surpasses the "standard" number of iterations (5,000) by an order of magnitude. Their FORC diagram exhibits multiple positive and negative features. However, the SF used was 5, which overly smooths the FORC function and creates averaging over several individual peaks, obscuring contributions from discreet irreversible events. In the present study we have used the smallest SF possible (2.5), in order to minimize these effects. The large SF used by Carvallo et al. (2003) thus renders their FORC diagram unsuitable for comparison with the diagrams presented here.

Roberts et al. (2017) provide the only other instance of finite-element micromagnetic modeling of SV FORCs for magnetite. These authors modeled a disk with a diameter of 240 nm and a thickness of 40 nm, and simulated FORC protocols with the field oriented at angles between 0° and 90° to the plane of the particle, in 5° increments. They noted that the main features of their FORC diagrams were two positive peaks of approximately the same coercivity, one in the upper half ($B_i > 0$) and one in the lower half ($B_i < 0$) of the FORC diagram, which they concluded should be taken as diagnostic signatures for particles in the vortex state. Upon closer inspection, their findings are more complex but are nevertheless consistent with our synthesis above. Each of their FORC protocols produced between two and four distinct FORC branches, with the lower branch intersecting the preceding branch in some cases. In their FORC diagrams, in addition to the two positive peaks, a pair of peaks are present in zone 3, one positive, contributing to the central ridge, and one negative. The only exceptions are in the 0° and 90° cases. For the 0° orientation, $B_{A+}^{V-} = B_{A+}^{V+}$, so the branches coincide at field values $>B_N^{V-}$. This creates the special case in which the FORC diagram contains no peaks in zone 3, and the two positive peaks in the upper and lower FORC half planes have the same coercivities (i.e., are equidistant from the B_i axis). For the 90° orientation, the only feature present is the positive peak on the central ridge, because of SD-like switching of the particle. For all other orientations, B_{A+}^{V-} is different from B_{A+}^{V+} (i.e., the branches do not coincide at field values $>B_N^{V-}$). If the lower branch does not intersect the preceding branch (as for e.g., the 60° orientation), the negative peak in zone 3 plots at B_i values <0 (i.e., below the central ridge), while the positive peak in the upper FORC half plane has a lower coercivity than the positive peak in the lower FORC half plane. If the lower branch intersects the preceding branch (as for e.g., the 30° orientation), the negative peak plots at B_i values >0 (i.e., above the central ridge), while the positive peak in the upper FORC half plane has a higher coercivity than the positive peak in the lower FORC half plane. For most orientations, $B_N^{V+}>0$ and $B_N^{V-}<0$, so the nucleation of $V+$ and $V-$ are transient events, and the two positive peaks plot in zones 1 and 2 of the FORC diagram. For some orientations (e.g., the 45°), $B_N^{V+}<0$ and $B_N^{V-}>0$, so the two peaks plot in zone 3, contributing to remanent magnetization.

Valdez-Grijalva (2018) has modeled the FORC behavior of SV greigite in multiple (85–500) random orientations for individual cuboctahedra 60–80 nm in size, and a framboidal aggregate (composed of tightly packed 30-nm SD particles) that exhibited super-vortex behavior. The averaged FORC diagram for the 60-80 nm SV particles have similar features to those described here (two positive lobes in each of the FORC half planes and a central ridge-like structure accompanied by a negative area below it), indicating that the SV FORC fingerprint is diagnostic for both magnetite and greigite. The central ridge-like structure is spread vertically across 10 mT and has a peak that is slightly offset from the horizontal axis in the negative direction. These effects are due to the fact that the greigite cuboctahedra are dominated by magnetocrystalline (rather than uniaxial) anisotropy. The cubic anisotropy creates other FORC signatures in addition to the ones already mentioned: a strong negative peak at low B_c and small negative B_i values, a weak negative region in the lower left of the FORC diagram, as well as positive and negative diagonal ridges along the lower diagonal. The greigite framboid composed of tightly-packed (but not touching) 30-nm SD particles was in a super-vortex state at remanence, but its FORC fingerprint was more akin to MD FORC signatures, with a low coercivity (<20 mT) vertical ridge extending to ±80 mT.

4.2. The MV Fingerprint and the MV-MD Transition

Egli and Winklhofer (2014) and Roberts et al. (2014, 2017) have suggested that SV features that average out over the FORC space may produce the central peak feature. However, lobe overlap cannot account for all the signal in the central peak area. In SV-dominated samples (e.g., dusty olivine Lappe et al., 2011, 2013, or hexagonal bacterial platelets Zhao et al., 2017), transient irreversible processes account for vortex nucleation events, resulting in upper and lower lobes that are confined mostly to zones 1 and 2 of the FORC diagram. No central peak is present in these samples, meaning that SV process alone do not explain the intensity of central peak in typical natural samples. To explain the central peak feature, MV processes must be invoked.

MV states have been previously documented through imaging and modeling, especially in the field of materials science (e.g., Donnelly et al., 2017; Elmurodov et al., 2006; Gan et al., 2014; Ivanov et al., 2016; Kanda et al., 2004; Xu et al., 2008) but also in the earth and planetary sciences (Einsle et al., 2016; Roberts et al., 2017; Shah et al., 2018). The key findings of these studies are that MV states are stable in natural and synthetic materials and that their remanent magnetizations are higher than for SV states. In natural materials, MV grains may carry stable magnetizations on time scales comparable to the age of the solar system (Shah et al., 2018).

No finite-element micromagnetic modeling of MV FORCs exists in the literature. With the present contribution we have taken the first step to fill this void. According to our simulations, MV features contribute mostly to zone 3, and subordinately to zones 1 and 2 of the FORC diagram. In zone 3, MV contributions are distinct from SV contributions in that they occur at lower coercivities, and are vertically spread, mapping onto the central peak feature. MV contributions to the central ridge occur only when there is inversion symmetry. This is conditioned by a lack of magnetostatic interactions, such as seen for particle gm5, which contains isolated vortices and uniformly magnetized regions that switch at the same absolute field value along the upper and lower hysteresis branches. This seems to be rare, however, since the central peak is broad, and asymmetric, with a maximum intensity displaced from the horizontal axis. Compared to SV particles, MV particles must be relatively abundant in geologic materials with predominantly vortex state grains, because the central peak has a relatively high intensity compared to that of the lobes.

The MV reversible and irreversible processes we have documented are core reorientations, translations, and their interactions, including merging of individual cores. As the field is decreased along the upper hysteresis branch, we have observed that in general, in positive fields, irreversible events contribute to the decrease of net magnetization to a lesser degree than in the case of SV simulations. This is likely due to MV intraparticle interactions between individual vortices, or between vortices and uniformly magnetized regions of a particle. The compound effect of these interactions is that, with decreasing field, the system reaches the sequence of major irreversible events after the particle has passed through zero field, resulting in high M_{rs}/M_s values (Table 1 and Figure 8b). The largest jumps tend to occur in negative fields, especially in easy magnetic directions, and switch back in positive fields (i.e., they are not transient events). Thus, irreversible events occurring along FORC branches starting at negative B_r values will contribute to zone 3 of the FORC diagram. This mechanism provides an explanation for the SD-like remanent magnetizations of MV particles.

The MV fingerprint in FORC diagrams indicates that MV-dominated particles are fundamentally different from MD particles. MD FORC fingerprints spread along the B_i axis at very low coercivities, whereas MV FORC diagrams resemble those of interacting SD particles, which also exhibit a broad peak in zone 3 (Harrison & Lascu, 2014; Muxworthy & Williams, 2005). The transition from MV to MD occurs when the particle is large enough, and with a sufficiently large number of micromagnetic states it can adopt, that a transition from step-wise to gradual decrease in magnetization occurs as the field is decreased from saturation. In this transitional state, domain walls will coexist with vortex cores; this occurs for particle sizes starting at around 1 μm in equidimensional magnetite (Nagy et al., 2017; Roberts et al., 2017). The particles we have modeled are defect-free, with only shape anisotropy influencing the magnetization states. Natural samples usually have defects, which can pin domain walls or vortex cores in transitional MV-MD particles. Defects may divide a MD particle into smaller regions, some of which will behave effectively like individual vortex particles. The coexistence of domains and SV-like regions may explain the FORC signature of natural MD particles, which retains elements of the tri-lobate geometry characteristic of SV signatures. This may also explain why FORC diagrams of materials dominated by MD behavior often exhibit a more pronounced negative region between the lower and middle lobe than in the case of MV-dominated samples (e.g., Wright Co. magnetite 3006, with a mean particle size of 1 μm; Yu, 2002), which may lack a negative region altogether.

Finally, we caution against the use of the Day diagram (Day et al., 1977) to diagnose systems containing vortex particles. As can be seen in Figure 8b, the MV grains used in the simulations exhibit hysteresis parameters that plot towards the upper left corner, in the general area classically attributed to SD grains. In contrast, hysteresis parameters for the SV simulations plot in the lower right corner, in the region designated for MD particles. For vortex state particles we thus witness an opposite grain size trend to that expected from a Day diagram. For comparison, the hysteresis parameters of bulk obsidian samples plot in the PSD region, suggesting a mixture of SV and MV characteristics. MV particles are abundant in rocks and could be the prime natural remanent magnetization carriers in geologic materials. The next logical step would be to determine their stability as remanence recorders. A number of factors will contribute to this, including particle shape, structural defects, the number and locations of vortex cores, field direction, magnetization history, and thermal fluctuations. These factors will determine the occurrence and thermal stability of local energy minima and the magnitude of associated energy barriers.

5. Conclusions

1. We have provided a detailed understanding of vortex-related phenomena in geologic materials by simulating FORCs using finite-element micromagnetic modeling of magnetite nanoparticles with realistic morphologies. The particles have been reconstructed from FIB-nanotomography of magnetite-bearing obsidian, and vary in size from 100 nm to >1μm, accommodating single and multiple vortex structures. Micromagnetic modeling of particles with realistic shapes show that modeling vortex phenomena using overly simplistic models (e.g., double hysteron) are inadequate in understanding vortex behavior.
2. Positive and negative features in the FORC diagram result from the evaluation of the slopes of two successive FORCs. If the slope of a FORC is greater (lesser) than that of the preceding FORC, indicating a higher (lower) rate of change for the magnetization as a function of field, the FORC function will be positive (negative). Gradual slope changes will result in elongated features in the FORC diagram, whereas sudden slope changes, caused by irreversible magnetization jumps, will translate as point peaks.
3. SV grains have FORC fingerprints with contributions in both the transient and transient-free zones of the FORC diagram. A fundamental feature of the SV fingerprint is a central ridge, accompanied by a negative trough below it. This stems from individual noninteracting SV grains contributing positive peaks along the coercivity axis of the FORC diagram, which are preceded by negative peaks. The positive-negative pairing occurs due to V^- annihilating along the lower hysteresis branch at a higher field value than V^+ along the preceding FORC branch. SV central ridges are thus distributions of V^- annihilation fields, and usually have higher median coercivities than SD central ridges, which are distributions of SD switching fields. SV nucleation-annihilation events at multiple field values along different branches (caused mainly by the annihilation of V^+ and V^- on different sides of the particle) also determine the asymmetry in the upper and lower lobes of generic bulk FORC diagrams of natural materials with grains predominantly in the vortex state.
4. We have modeled MV FORC signatures for the first time. MV grains contribute mostly to the transient-free zone of a FORC diagram. Due to their larger size, multiple micromagnetic states they can adopt, and intraparticle interactions, MV grains contribute positive and negative peaks that are spread vertically, which for large populations of particles average out to create the broad central peak in the FORC diagram. The intensity of the central peak is generally higher than that of the lobes, implying that MV particles are more abundant than SV particles in geologic materials with vortex state fingerprints. This is of high importance because MV grains could then be the prime natural remanent magnetization carriers in rocks. Finally, based on the similarities between the FORC fingerprints of strongly interacting SD and MV particles, we propose that widely documented SD-like moments in geologic vortex state samples are due to MV, not SD grains.

Acknowledgments
This research has received funding from the European Research Council under the European Union's Seventh Framework Programme (FP/2007-2013)/ERC grant agreement 320750. The mesh files used to generate the data in this paper are available as supporting information. We thank James A. Miller for providing the obsidian specimens and Wyn Williams for assistance with MERRILL. We are grateful to Ramon Egli, Adrian Muxworthy, Valera Shcherbakov, and Lesleis Nagy for providing constructive reviews that improved the quality of this paper.

References

Ahrens, J., Geveci, B., & Law, C. (2005). Paraview: An end-user tool for large-data visualization. In C. Hansen & C. Johnson (Eds.), *The Visualization Handbook* (pp. 717–732). Jordan Hill, Oxford: Elsevier.

Almeida, T. P., Muxworthy, A. R., Kovács, A., Williams, W., Brown, P. D., & Dunin-Borkowski, R. E. (2016). Direct visualization of the thermomagnetic behavior of pseudo-single-domain magnetite particles. *Science Advances*, *2*(4). https://doi.org/10.1126/sciadv.1501801

Ambroz, J. A., Glascock, M. D., & Skinner, C. E. (2001). Chemical differentiation of obsidian within the Glass Buttes complex, Oregon. *Journal of Archaeological Science*, *28*(7), 741–746. https://doi.org/10.1006/jasc.2000.0593

Carter-Stiglitz, B., Moskowitz, B., & Jackson, M. (2001). Unmixing magnetic assemblages and the magnetic behavior of bimodal mixtures. *Journal of Geophysical Research*, *106*(B11), 26,397–26,411. https://doi.org/10.1029/2001JB000417

Carvallo, C., Muxworthy, A. R., & Dunlop, D. J. (2006). First-order reversal curve (FORC) diagrams of magnetic mixtures: Micromagnetic models and measurements. *Physics of the Earth and Planetary Interiors*, *154*(3), 308–322. https://doi.org/10.1016/j.pepi.2005.06.017

Carvallo, C., Muxworthy, A. R., Dunlop, D. J., & Williams, W. (2003). Micromagnetic modeling of first-order reversal curve (FORC) diagrams for single-domain and pseudo-single-domain magnetite. *Earth and Planetary Science Letters*, *213*(3-4), 375–390. https://doi.org/10.1016/S0012-821X(03)00320-0

Day, R., Fuller, M., & Schmidt, V. (1977). Hysteresis properties of titanomagnetites: Grain-size and compositional dependence. *Physics of the Earth and Planetary Interiors*, *13*(4), 260–267. https://doi.org/10.1016/0031-9201(77)90108-X

Donnelly, C., Guizar-Sicairos, M., Scagnoli, V., Gliga, S., Holler, M., Raabe, J., et al. (2017). Three-dimensional magnetization structures revealed with X-ray vector nanotomography. *Nature*, *547*, 328–331. https://doi.org/10.1038/nature23006

Dumas, R. K., Gredig, T., Li, C.-P., Schuller, I. K., & Liu, K. (2009). Angular dependence of vortex-annihilation fields in asymmetric cobalt dots. *Physical Review B*, *80*(014), 416. https://doi.org/10.1103/PhysRevB.80.014416

Dumas, R. K., Li, C.-P., Roshchin, I. V., Schuller, I. K., & Liu, K. (2007). Magnetic fingerprints of sub-100 nm fe nanodots. *Physical Review B*, *75*(134), 405. https://doi.org/10.1103/PhysRevB.75.134405

Dumas, R. K., Li, C.-P., Roshchin, I. V., Schuller, I. K., & Liu, K. (2012). Deconvoluting reversal modes in exchange-biased nanodots. *Physical Review B*, *86*(144), 410. https://doi.org/10.1103/PhysRevB.86.144410

Dumas, R. K., Liu, K., Li, C.-P., Roshchin, I. V., & Schuller, I. K. (2007). Temperature induced single domain–vortex state transition in sub-100 nm fe nanodots. *Applied Physics Letters*, *91*(20), 202–501. https://doi.org/10.1063/1.2807276

Dunlop, D. J., & Carter-Stiglitz, B. (2006). Day plots of mixtures of superparamagnetic, single-domain, pseudosingle-domain, and multidomain magnetites. *Journal of Geophysical Research*, *111*, B12S09. https://doi.org/10.1029/2006JB004499

Egli, R. (2013). VARIFORC: An optimized protocol for calculating non-regular first-order reversal curve (FORC) diagrams. *Global and Planetary Change*, *110*, 302–320. https://doi.org/10.1016/j.gloplacha.2013.08.003

Egli, R., & Winklhofer, M. (2014). Recent developments on processing and interpretation aspects of first-order reversal curves (FORC). *Proceedings of Kazan University*, *156*, 14–53.

Einsle, J. F., Harrison, R. J., Kasama, T., Ó Conbhuí, P., Fabian, K., Williams, W., et al. (2016). Multi-scale three-dimensional characterization of iron particles in dusty olivine: Implications for paleomagnetism of chondritic meteorites. *American Mineralogist*, *101*(9), 2070–2084. https://doi.org/10.2138/am-2016-5738CCBY

Elmurodov, A. K., Vodolazov, D. Y., & Peeters, F. M. (2006). The break-up of the vortex structure in a mesoscopic wire containing a constriction. *Europhysics Letters*, *74*(1), 151. https://doi.org/10.1209/epl/i2005-10496-0

Fabian, K. (2003). Some additional parameters to estimate domain state from isothermal magnetization measurements. *Earth and Planetary Science Letters*, *213*(3), 337–345. https://doi.org/10.1016/S0012-821X(03)00329-7

Fabian, K., & von Dobeneck, T. (1997). Isothermal magnetization of samples with stable Preisach function: A survey of hysteresis, remanence, and rock magnetic parameters. *Journal of Geophysical Research*, *102*(B8), 17,659–17,677. https://doi.org/10.1029/97JB01051

Fang, Q., & Boas, D. A. (2009). Tetrahedral mesh generation from volumetric binary and grayscale images. In *From Nano to Macro 2009 IEEE International Symposium on Biomedical Imaging* (pp. 1142–1145). https://doi.org/10.1109/ISBI.2009.5193259

Frahm, E., & Feinberg, J. M. (2015). Reassessing obsidian field relationships at Glass Buttes, Oregon. *Journal of Archaeological Science: Reports*, *2*, 654–665. https://doi.org/10.1016/j.jasrep.2014.11.007

Gan, W. L., Sekhar, M. C., Wong, D. W., Purnama, I., Chiam, S. Y., Wong, L. M., et al. (2014). Multi-vortex states in magnetic nanoparticles. *Applied Physics Letters*, *105*(15), 152405. https://doi.org/10.1063/1.4898349

Harrison, R. J., & Feinberg, J. M. (2008). FORCinel: An improved algorithm for calculating first-order reversal curve distributions using locally weighted regression smoothing. *Geochemistry, Geophysics, Geosystems*, *9*(5), Q05016. https://doi.org/10.1029/2008GC001987

Harrison, R. J., & Lascu, I. (2014). FORCulator: A micromagnetic tool for simulating first-order reversal curve diagrams. *Geochemistry, Geophysics, Geosystems*, *15*(12), 4671–4691. https://doi.org/10.1002/2014GC005582

Harrison, R. J., Muraszko, J., Heslop, D., Lascu, I., Muxworthy, A. R., & Roberts, A. P. (2018). An improved algorithm for unmixing first-order reversal curve diagrams using principal component analysis. *Geochemistry, Geophysics, Geosystems*, *19*, 1595–1610. https://doi.org/10.1029/2018GC007511

Heslop, D., & Roberts, A. P. (2012). A method for unmixing magnetic hysteresis loops. *Journal of Geophysical Research*, *117*, B03103. https://doi.org/10.1029/2011JB008859

Ivanov, Y. P., Chuvilin, A., Vivas, L. G., Kosel, J., Chubykalo-Fesenko, O., & Vázquez, M. (2016). Single crystalline cylindrical nanowires–toward dense 3D arrays of magnetic vortices. *Scientific Reports*, *6*(23), 844. https://doi.org/10.1038/srep23844

Jones, H., Mingard, K., & Cox, D. (2014). Investigation of slice thickness and shape milled by a focused ion beam for three-dimensional reconstruction of microstructures. *Ultramicroscopy*, *139*, 20–28. https://doi.org/10.1016/j.ultramic.2014.01.003

Kanda, A., Baelus, B. J., Peeters, F. M., Kadowaki, K., & Ootuka, Y. (2004). Experimental evidence for giant vortex states in a mesoscopic superconducting disk. *Physical Review Letters*, *93*(257), 002. https://doi.org/10.1103/PhysRevLett.93.257002

Lappe, S.-C. L. L., Church, N. S., Kasama, T., da Silva Fanta, A. B., Bromiley, G., Dunin-Borkowski, R. E., et al. (2011). Mineral magnetism of dusty olivine: A credible recorder of pre-accretionary remanence. *Geochemistry, Geophysics, Geosystems*, *12*, Q12Z35. https://doi.org/10.1029/2011GC003811

Lappe, S.-C. L. L., Feinberg, J. M., Muxworthy, A., & Harrison, R. J. (2013). Comparison and calibration of nonheating paleointensity methods: A case study using dusty olivine. *Geochemistry, Geophysics, Geosystems*, *14*(7), 2143–2158. https://doi.org/10.1002/ggge.20141

Ludwig, P., Egli, R., Bishop, S., Chernenko, V., Frederichs, T., Rugel, G., et al. (2013). Characterization of primary and secondary magnetite in marine sediment by combining chemical and magnetic unmixing techniques. *Global and Planetary Change*, *110*, 321–339. https://doi.org/10.1016/j.gloplacha.2013.08.018

Ma, C., Rossman, G. R., & Miller, J. A. (2007). The origin of color in "fire" obsidian. *Canadian Mineralogist*, *45*, 551–557. https://doi.org/10.2113/gscanmin.45.3.551

Muxworthy, A., & Williams, W. (2005). Magnetostatic interaction fields in first-order-reversal-curve diagrams. *Journal of Applied Physics*, *97*(6), 063905. https://doi.org/10.1063/1.1861518

Nagy, L., Williams, W., Muxworthy, A. R., Fabian, K., Almeida, T. P., Ó Conbhuí, P., et al. (2017). Stability of equidimensional pseudo–single-domain magnetite over billion-year timescales. *Proceedings of the National Academy of Sciences*, *114*(39), 10,356–10,360.

Néel, L. (1949). Théorie du trainage magnétique des ferromagnétiques en grains fines avec applications aux terres cuites. *Annales de Géophysique*, *5*, 99–136.

Ó Conbhuí, P., Williams, W., Fabian, K., Ridley, P., Nagy, L., & Muxworthy, A. R. (2018). MERRILL: Micromagnetic earth related robust interpreted language laboratory. *Geochemistry, Geophysics, Geosystems*, *19*(4), 1080–1106. https://doi.org/10.1002/2017GC007279

Pike, C., & Fernandez, A. (1999). An investigation of magnetic reversal in submicron-scale Co dots using first order reversal curve diagrams. *Journal of Applied Physics*, *85*(9), 6668–6676. https://doi.org/10.1063/1.370177

Pike, C. R., Roberts, A. P., & Verosub, K. L. (1999). Characterizing interactions in fine magnetic particle systems using first order reversal curves. *Journal of Applied Physics*, *85*(9), 6660–6667.

Roberts, A. P., Almeida, T. P., Church, N. S., Harrison, R. J., Heslop, D., Li, Y., et al. (2017). Resolving the origin of pseudo-single domain magnetic behavior. *Journal of Geophysical Research: Solid Earth*, *122*, 9534–9558. https://doi.org/10.1002/2017JB014860

Roberts, A. P., Heslop, D., Zhao, X., & Pike, C. R. (2014). Understanding fine magnetic particle systems through use of first-order reversal curve diagrams. *Reviews of Geophysics*, *52*(4), 557–602. https://doi.org/10.1002/2014RG000462

Roberts, A. P., Pike, C. R., & Verosub, K. L. (2000). First-order reversal curve diagrams: A new tool for characterizing the magnetic properties of natural samples. *Journal of Geophysical Research*, *105*(B12), 28,461–28,475. https://doi.org/10.1029/2000JB900326

Shah, J., Williams, W., Almeida, T. P., Nagy, L., Muxworthy, A. R., Kovács, A., et al. (2018). The oldest magnetic record in our solar system identified using nanometric imaging and numerical modeling. *Nature Communications*, *9*(1), 1173. https://doi.org/10.1038/s41467-018-03613-1

Shcherbakov, V., Schmidt, P., Sycheva, N., & Lamash, B. (1990). Micromagnetic formulation for the personal computer. *Physics of the Earth and Planetary Interiors*, *65*(1), 15–27. https://doi.org/10.1016/0031-9201(90)90071-5

Smirnov, A. V., & Evans, D. A. (2015). Geomagnetic paleointensity at 2.41 Ga as recorded by the Widgiemooltha Dike Swarm, Western Australia. *Earth and Planetary Science Letters*, *416*, 35–45. https://doi.org/10.1016/j.epsl.2015.02.012

Stacey, F. D. (1962). A generalized theory of thermoremanence, covering the transition from single domain to multi-domain magnetic grains. *Philosophical Magazine*, *7*(83), 1887–1900. https://doi.org/10.1080/14786436208213853

Stacey, F. (1963). The physical theory of rock magnetism. *Advances in Physics*, *12*(45), 45–133. https://doi.org/10.1080/00018736300101263

Valdez-Grijalva, M. A. (2018). A numerical investigation of hydrocarbon related magnetic signatures (Ph.D. thesis), Imperial College London.

Williams, W., & Dunlop, D. J. (1995). Simulation of magnetic hysteresis in pseudo-single-domain grains of magnetite. *Journal of Geophysical Research*, *100*(B3), 3859–3871. https://doi.org/10.1029/94JB02878

Winklhofer, M., Dumas, R. K., & Liu, K. (2008). Identifying reversible and irreversible magnetization changes in prototype patterned media using first- and second-order reversal curves. *Journal of Applied Physics*, *103*(7), 07C518. https://doi.org/10.1063/1.2837888

Xu, B., Milošević, M. V., & Peeters, F. M. (2008). Magnetic properties of vortex states in spherical superconductors. *Physical Review B*, *77*(144), 509. https://doi.org/10.1103/PhysRevB.77.144509

Yu, Y. (2002). Partial anhysteretic remanent magnetization in magnetite 1. Additivity. *Journal of Geophysical Research*, *107*(B10), 2244. https://doi.org/10.1029/2001JB001249

Zhao, X., Roberts, A. P., Heslop, D., Paterson, G. A., Li, Y., & Li, J. (2017). Magnetic domain state diagnosis using hysteresis reversal curves. *Journal of Geophysical Research: Solid Earth*, *122*, 4767–4789. https://doi.org/10.1002/2016JB013683